ACS APPLIED ENERGY MATERIALS
Cite This: ACS Appl. Energy Mater. 2018, 1, 5417−5427
Article
www.acsaem.org

3D Copper Foam@FeO_x Nanoarrays as a High Areal Capacity and Stable Electrode for Lithium-Ion Batteries

Feng Zhang,‡ Chengkai Yang,‡ Huanqin Guan, Yiran Hu, Can Jin, Henghui Zhou,* and Limin Qi*

Beijing National Laboratory for Molecular Sciences (BNLMS), College of Chemistry, Peking University, Beijing 100871, China

Supporting Information

ABSTRACT: Despite remarkable development in high capacity iron oxide-based electrodes for lithium-ion batteries (LIBs), the low mass loading and poor areal capacity still impede their practical applications. In this report, novel FeO_x nanoarrays were directly constructed on three-dimensional (3D) copper foam current collector (denoted as CF@FeO_x NAs) via facile hydrothermal growth followed by a postannealing process. The nanoarrays were stacked by numerous FeO_x porous nanoblocks, exhibiting a unique hierarchical structure. The loading density of FeO_x in the CF@FeO_x NAs reached 2.5 mg cm^{-2} owing to the hierarchical structure of the novel 3D nanoarray electrode. When tested as an anode for LIBs, the 3D integrated electrode delivered high areal capacities of 3.33 and 2.61 mAh cm^{-2} at 0.25 and 1.25 mA cm^{-2}, respectively. A high areal capacity of 2.12 mAh cm^{-2} was retained at 2.5 mA cm^{-2} after 500 cycles, which is the best electrochemical performance in terms of areal capacity for the iron oxide-based electrodes reported so far. Even at a higher current density of 12.5 mA cm^{-2}, the areal capacity was still maintained at 0.96 mAh cm^{-2}, demonstrating good rate capability. A lithium full cell test was also conducted using $LiNi_{0.8}Co_{0.05}Al_{0.15}$ (NCA) as a cathode and the CF@FeO_x NAs as an anode, which exhibited a good areal capacity of 0.94 mAh cm^{-2} at 2.5 mA cm^{-2} after 50 cycles. This work offers a promising pathway to greatly enhance the loading density and areal capacity of metal oxide-based electrodes for electrochemical energy storage.

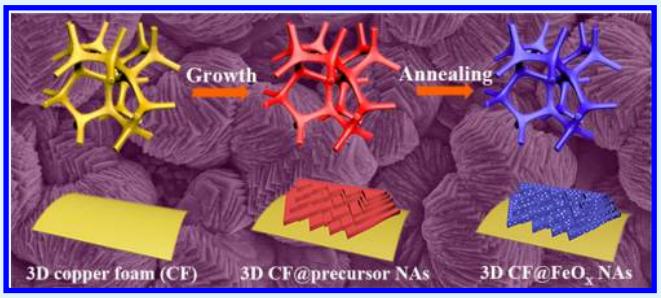

KEYWORDS: *iron oxide, nanoarrays, copper foam, areal capacity, lithium-ion batteries*

1. INTRODUCTION

To meet the development of rapidly upgrading new energy vehicles, lithium ion batteries (LIBs) with large energy density, high power density, and long lifespan are of great technological importance.[1−3] However, the current commercialized graphite anode suffers from low theoretical capacity (372 mAh g^{-1}) and poor rate performance, which hinders their practical utilization in large-scale devices.[4] Transition metal oxides (TMOs) have been considered as promising anode materials in LIBs for more than a decade, since they can provide much higher capacities based on the conversion reaction mechanism compared with graphite.[5,6] As a typical kind of TMOs, iron oxides, such as Fe_2O_3 and Fe_3O_4, have long been investigated as promising candidates for next-generation LIB anodes because of their natural abundance, nontoxicity, low cost, and high theoretical capacities.[7,8] Nevertheless, several general obstacles still exist for iron oxides as anode materials for LIBs and greatly compromise their electrochemical performance.[9−12] First, the drastic volume expansion and contraction during lithiation and delithiation processes cause pulverization and aggregation of iron oxides, which results in the capacity decay and short cycle life. Second, the inferior electron transport and lithium ion diffusion efficiency arising from poor intrinsic charge transfer abilities of iron oxides are harmful for the rate capability. Beyond that, the lack of continuous conductive network inside the electrode often leads to the low utilization of active materials. Therefore, there is an urgent demand for rational design and fabrication of high-performance iron oxide-based electrodes.

To solve these problems, two reasonable strategies have been successfully employed to develop novel iron oxide electrodes. The first is constructing a variety of hierarchical micro- and nanostructures, which has been frequently employed for iron oxides[13−19] as well as other electrode materials.[20−29] With rational designs, the lithium ion transport can be accelerated because of the reduced diffusion lengths. Besides, the empty space inside the hierarchical skeleton is beneficial to alleviate the huge volume change to maintain the structural integrity of electrodes. For example, Lou and co-workers synthesized highly uniform hierarchical Fe_3O_4 hollow spheres consisting of ultrathin porous nanosheets, leading to an LIB anode with a high capacity of 1046 mAh g^{-1} achieved after 100 cycles at 0.5 A g^{-1}.[30] The second efficient approach is filling iron oxides into a 3D conductive carbonaceous framework,[31−36] similar to the incorporation of other active materials into carbonaceous frameworks.[37] During the charge−

Received: June 24, 2018
Accepted: September 12, 2018
Published: September 12, 2018

DOI: 10.1021/acsaem.8b01024
ACS Appl. Energy Mater. 2018, 1, 5417−5427

discharge processes, the carbon materials not only act as a conductive matrix to enhance the conductivity, but also act as a buffer material to relieve the pulverization. As a typical example, Jiang et al. produced a 3D graphene/Fe_2O_3 aerogel with porous Fe_2O_3 nanoframeworks well encapsulated within graphene skeleton, which delivered a capacity of 523.5 mAh g^{-1} after 1200 cycles at 5 A g^{-1}, demonstrating superior electrochemical properties.[38]

Despite improved performance of iron oxide electrodes in terms of gravimetric capacity, it remains a challenge to achieve practical applications. In particular, the mass loading of iron oxides is an indispensable factor that should be seriously taken into consideration. Although high gravimetric capacities have been reported for a variety of iron oxide electrodes, their areal capacities, which have close relation to the whole energy of the batteries, are still insufficient due to the low mass loading of active materials.[17,18,30,39−43] Generally, a basic method to enhance the areal capacity of an electrode is to increase the thickness of the iron oxide film tapping cast on the current collector. Nevertheless, the electron transport resistance is in turn greatly enhanced due to the increased transportation lengths and the number of grain boundaries, leading to the recession of the electrochemical performance.[44] Hence, it is of great significance to increase the loading density of active materials without significantly enhancing electron transport resistance. To this end, constructing active materials directly on current collector to form a binder-free nanoarray electrode represents an effective approach toward high areal capacity, because the good contact between active materials and current collector and the lack of binders offer direct pathways for electron transport, generating a high electron transport efficiency and improved electrochemical performance.[43,45−49] For instance, we fabricated self-supported α-Fe_2O_3 nanorod arrays made of mesocrystalline nanorod bundles through hydrothermal growth followed by chemical etching.[50] The optimized α-Fe_2O_3 nanorod arrays exhibited excellent rate capability with a capacity of 970 mAh g^{-1} retained after 130 cycles at 5 C, and a good capacity of 350 mAh g^{-1} at a high current density of 30 C was maintained. It is noteworthy that hierarchical porous α-Fe_2O_3 nanosheet arrays were fabricated on copper foil and directly used as a binder-free anode for LIBs.[51] As a result, a much enhanced cycling stability with minimal capacity decaying (1001 mAh g^{-1} after 320 cycles at 1 C) and excellent rate capability (338.9 mAh g^{-1} at 20 C) were achieved. However, the low loading density of active material (0.35 mg cm^{-2}) arising from the limited growth sites offered by 2D plane copper foil resulted in a low areal capacity (0.355 mAh cm^{-2} after 320 cycles). In this regard, it is challenging to achieve iron oxide electrode with high loading density and desirable areal capacity via deliberate design of electrode architecture. For this purpose, constructing self-supported nanoarrays on 3D conductive substrates[46] provides an effective strategy to attain iron oxide electrodes with high loading density and enhanced areal capacity.

In this work, hierarchical porous iron oxide nanoarrays were directly fabricated on 3D copper foam (denoted as CF@FeO_x NAs) via facile hydrothermal growth and a postannealing process. In contrast to 2D plane copper foil, 3D copper foam with a considerably higher specific area provides more growth sites for active materials. As a consequence, the loading density of FeO_x in the CF@FeO_x NAs can be largely increased to 2.5 mg cm^{-2}. When tested as a binder-free anode for LIBs, the 3D CF@FeO_x NAs electrode demonstrated much enhanced areal capacities of 3.33 and 2.61 mAh cm^{-2} at current densities of 0.25 and 1.25 mA cm^{-2}, respectively. Impressively, a stable areal capacity of 2.12 mAh cm^{-2} at a current density of 2.5 mA cm^{-2} was delivered after 500 cycles, indicating excellent cycling performance. Besides, an areal capacity of 0.96 mAh cm^{-2} was achieved at a high current density of 12.5 mA cm^{-2}, indicating a good rate capability. To evaluate the potential for practical utilization, a lithium full cell test was also conducted using $LiNi_{0.8}Co_{0.05}Al_{0.15}$ (NCA) as a cathode and the 3D CF@FeO_x NAs as an anode. A high areal capacity of 0.94 mAh cm^{-2} was achieved after 50 cycles at 2.5 mA cm^{-2}, demonstrating favorable potential for practical applications.

2. EXPERIMENTAL SECTION

2.1. Materials. Copper foam (0.5 mm in thickness) was purchased from Suzhou Taili Foam Metal Factory. $FeSO_4·7H_2O$ (99.0%) was obtained from Sinopharm Chemical Reagent Co., Ltd. Urea (≥99.0%), NH_4F (≥99.0%) and hydrochloric acid (36.0−38.0%) were from Xilong Chemical Co., Ltd. Ethanol (99.7%) was from Beijing Tongguang Fine Chemicals Company. The hydroiodic acid (55.0−58.0%) was purchased from Aladdin. Deionized (DI) water was used.

2.2. Synthesis of 3D CF@precursor NAs. The copper foam was cut to a size of 1 cm × 2.5 cm, rinsed by sonication in 1 M HCl, water, and ethanol, and finally dried in air before reaction. $FeSO_4·7H_2O$ (0.6 g), urea (0.2 g), and NH_4F (0.05 g) were dissolved in 10 mL of water under stirring in an ice−water bath for 10 min, giving a deep yellow solution. The solution was then transferred into a Teflon-lined stainless steel autoclave (25 mL), where the pretreated copper foam was fixed at an angle (typically ∼30°) against the inner wall. After it was kept at 100 °C for 14 h, the autoclave was cooled to room temperature. The obtained copper foam was rinsed with water and ethanol successively and dried at 70 °C overnight.

2.3. Synthesis of 3D CF@FeO_x NAs. The as-prepared 3D CF@precursor NAs was put in the center of a tube furnace (SK2-2.5-13A, Tianjin Zhonghuan Electronic and information Co., Ltd.) and annealed at 450 °C with a temperature rise rate of 5 °C min^{-1} in Ar for 2 h to obtain 3D CF@FeO_x NAs. For the investigation of the effects of the annealing time, 3D CF@FeO_x NAs-1 and 3D CF@FeO_x NAs-3 were obtained when the annealing time was changed to 1 and 3 h, respectively. For comparison purposes, FeO_x precursor powder was fabricated via a similar hydrothermal process without the addition of 3D copper foam substrate in the autoclave. The resultant powder was separated by centrifugation, washed with water and ethanol several times. The final FeO_x powder was obtained after annealing at 450 °C in Ar for 2 h with a temperature rise rate of 5 °C min^{-1}. The mass loading of FeO_x for 3D CF@FeO_x NAs was measured by immersing the electrode into an aqueous HI solution with a 1:10 volume ratio of HI and H_2O to dissolve the FeO_x. By measuring the mass change of the electrode before and after the dissolution, the loading density of FeO_x was calculated to be 2.5 mg cm^{-2}.

2.4. Characterizations. X-ray diffraction (XRD) measurements were conducted with a Rigaku Dmax-2000 diffractometer using Cu Kα radiation. Raman spectra were obtained with a Horiba HR800 spectrometer. Scanning electron microscopy (SEM) was conducted on a Hitachi S4800 microscope equipped with energy-dispersive spectroscopy (EDS), and transmission electron microscopy (TEM) was performed on an FEI Tecnai F30 microscope. Inductively Coupled Plasma-Atomic Emission Spectrometer (ICP-AES, Leeman, Profile Spec) was used to measure the concentration of iron and copper ions in solutions. Nitrogen adsorption−desorption measurements were performed on a Quadrasorb SI-MP instrument. The specific surface area was calculated by the Brunauer−Emmett−Teller (BET) method, and the pore-size distribution curve was determined from the desorption isotherm using the Barrett−Joyner−Halenda (BJH) method.

2.5. Electrochemical Measurements. The 3D CF@FeO_x NAs, together with CF@FeO_x NAs-1 and CF@FeO_x NAs-3, were cut into

DOI: 10.1021/acsaem.8b01024
ACS Appl. Energy Mater. 2018, 1, 5417−5427

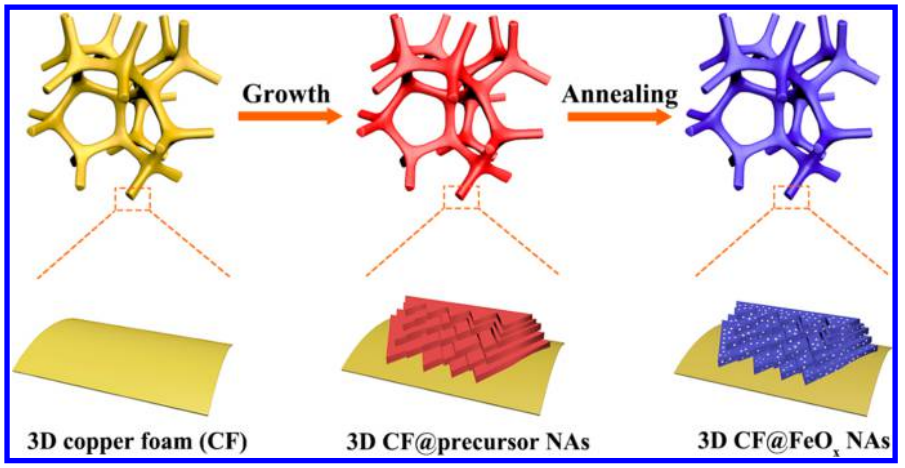

Figure 1. Schematic illustration of the fabrication process of 3D CF@FeO$_x$ NAs electrode.

1 cm × 1 cm, which were directly used as anodes and assembled in a 2032 coin cell with pure lithium foil as the counter electrode in an argon-filled glovebox. One molar lithium hexafluorophosphate ($LiPF_6$) in mixed solvents of ethylene carbonate, ethyl methyl carbonate, and dimethyl carbonate (1:1:1 in volume ratio) was used as electrolyte and Celgard 2400 was employed as the separator. For comparison purposes, a FeO$_x$ powder electrode with a loading density of 2.5 mg cm^{-2} was fabricated by casting the FeO$_x$ powder mixed with poly(vinylidene fluoride) (PVDF) binder and conductive carbon black (8:1:1, weight ratio) on Cu foil, which was dried in a vacuum oven for 12 h. The electrochemical performance was tested by using LAND CT2001A battery test system at room temperature (25 °C). The coin cells were discharged and charged between 3.0 and 0.05 V at a constant current. The cyclic voltammetry (CV) study was carried out on a CV autolab (Eco Chemie, PGSTAT302N). The electrochemical impedance spectroscopy (EIS) measurements were performed with an electrochemical workstation (CHI 660D, Shanghai Chenhua) in the frequency range 10^{-2}−10^5 Hz. For the full cell test, homemade $LiNi_{0.8}Co_{0.15}Al_{0.05}$ (NCA) mixed with PVDF binder and conductive carbon black (8:1:1, weight ratio) was coated on Al foil as cathode.[52] The mass ratio of the cathode to anode was controlled to be 10:1 in the full cell. The NCA electrode was fabricated into 2032 coin cell as the cathode with 3D CF@FeO$_x$ NAs as the anode. The voltage window of the full cell is 1.0−3.75 V.

3. RESULTS AND DISCUSSION

The synthetic route toward 3D CF@FeO$_x$ NAs is schematically illustrated in Figure 1, which includes the hydrothermal growth of FeO$_x$ precursor nanoarrays on CF to form 3D CF@precursor NAs, and the subsequent conversion into 3D CF@FeO$_x$ NAs. Typically, a piece of 3D CF was placed in 10 mL of aqueous solution containing $FeSO_4{\cdot}7H_2O$ (0.6 g), urea (0.2 g), and NH_4F (0.05 g) to undergo hydrothermal growth for 14 h. The resultant 3D CF@precursor NAs were annealed at 450 °C in Ar for 2 h, leading to the formation of the 3D CF@FeO$_x$ NAs. The morphology and microstructure of the obtained 3D CF@precursor NAs were characterized by SEM and TEM (Figure 2). As shown in Figure 2a, the hydrothermal growth of the FeO$_x$ precursor nanoarrays did not destroy the pristine structure of the CF made of macroporous skeleton. After the hydrothermal process, the surface of the CF is coated uniformly with densely aligned granules ∼5 μm in size, as shown in Figure 2b. The enlarged images displayed in Figure 2c and 2d suggest that each granule is stacked by numerous ordered nanoblocks with a thickness of ∼150 nm, and each nanoblock has smooth surfaces and sharp edges, indicating a hierarchical nanoarray structure. Figure 2e shows a typical

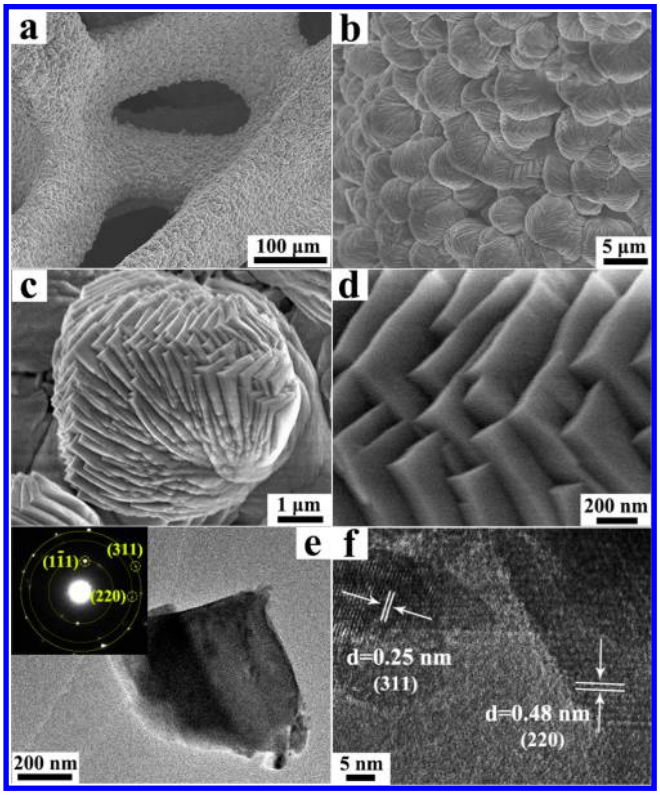

Figure 2. (a−d) SEM images of 3D CF@precursor NAs at different magnifications. TEM (e) and HRTEM (f) images of precursor nanoblocks. Inset shows the corresponding SAED pattern. The diffraction spots in (e) and the lattice fringes in (f) are indexed based on the Fe_3O_4 phase.

TEM image of a scraped nanoblock, and the related selected area electron diffraction (SAED) pattern exhibits sharp spots, which belong to the (1$\bar{1}$1), (220), and (311) planes of Fe_3O_4 with a face-centered cubic structure (JCPDS card no. 65-3107), indicating that the precursor block is mainly composed of a number of Fe_3O_4 subunit crystals with different orientations. The measured interlayer spacings of 0.25 and 0.48 nm corresponding to the (311) and (111) planes of the Fe_3O_4 phase can be observed from the HRTEM image in Figure 2f. However, the XRD pattern of the 3D CF@FeO$_x$ NAs was dominated by the sharp reflections from the copper foam substrate owing to the small content of the nanoarrays in

DOI: 10.1021/acsaem.8b01024
ACS Appl. Energy Mater. 2018, 1, 5417−5427

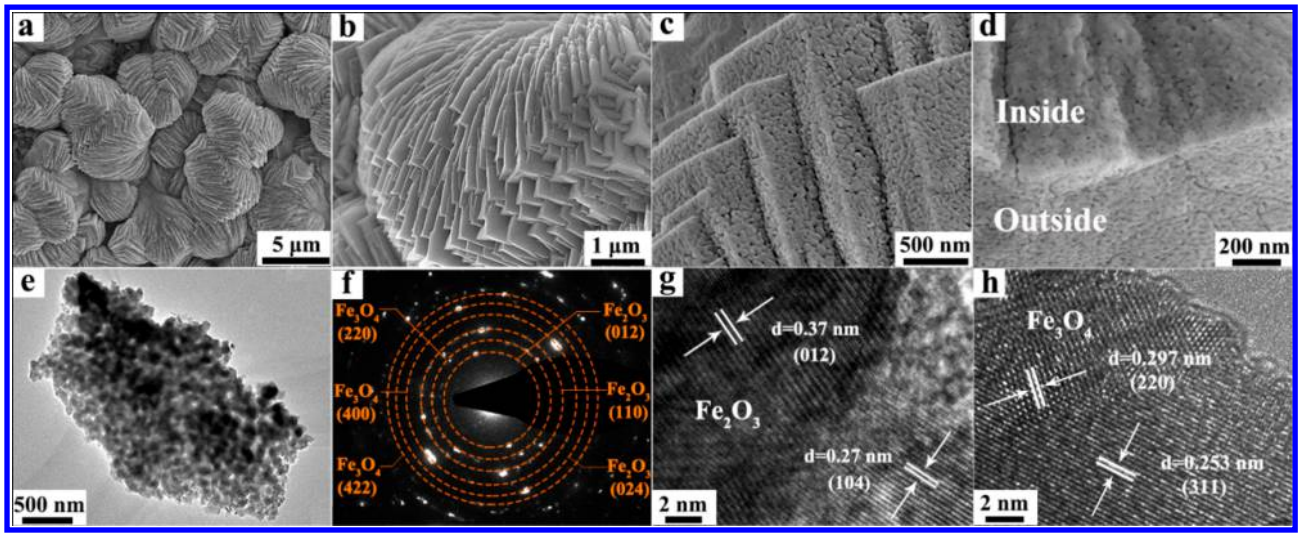

Figure 3. (a–d) SEM images of 3D CF@FeO_x NAs at different magnifications. TEM image (e) and the related SAED pattern (f) of a cracked FeO_x nanoblock. (g, h) HRTEM images of FeO_x nanoblocks.

the CF@FeO_x NAs (Figure S1a). Therefore, the precursor powder prepared in the absence of the copper foam under otherwise identical synthesis conditions (Figure S2a) was used for the XRD measurement to determine the chemical composition of the precursor. It is revealed that besides the Fe_3O_4 phase, the precursor powder also contains a mixed FeOOH phases made of the tetragonal phase (JCPDS card no. 75-1594) and the orthorhombic phase (JCPDS card no. 81-462), as shown in Figure S1a. It may be noted that the diffraction spots from the FeOOH phases were hardly observed from the SAED pattern shown in Figure 2e, which could be attributed to the relatively weak diffraction intensity and significant overlap with the diffractions from the Fe_3O_4 crystals. Therefore, it may be reasonably inferred that the 3D CF@precursor NAs are mainly composed of one iron oxide phase (i.e., Fe_3O_4) resulting from the partial oxidation of Fe(II) in the reaction solution, and two different oxyhydroxide phases (namely, tetragonal and orthorhombic FeOOH) resulting from the thorough oxidation of Fe(II).[51] It is worth noting that there was no noticeable oxidation of copper substrate during the hydrothermal synthesis since $FeSO_4$ was employed as the Fe source in the solution.

After annealing at 450 °C in Ar atmosphere, the transformation from 3D CF@precursor NAs to 3D CF@FeO_x NAs occurred accompanying the loss of water. SEM and TEM characterizations of 3D CF@FeO_x NAs are shown in Figure 3. The structural integrity of the individual FeO_x granules is well preserved without crack and aggregation after the annealing process (Figure 3a and b), and each FeO_x granule is made of stacked nanoblocks, similar to the hierarchical nanoarray structure of the initial 3D CF@precursor NAs. Notably, Figure 3c exhibits that the FeO_x nanoblocks become highly porous, and each FeO_x nanoblock is composed of numerous nanoparticles ranging from tens to hundreds of nanometers in size. This may be attributed to the release of water during the annealing process. Figure 3d shows an SEM image of a cracked nanoblock, confirming that the interior of the FeO_x nanoblocks is also porous. The TEM image shown in Figure 3e also exhibits the highly porous structure of an individual FeO_x nanoblock. Nitrogen adsorption/desorption isotherm measurements were performed to investigate the surface area and porosity of the obtained 3D CF@FeO_x NAs (Figure S3). It was shown that the CF@FeO_x NAs had a specific surface area of 10.7 $m^2\ g^{-1}$ with the total mass of the active material, similar to that of the reported 3D porous Ni–Co layered double hydroxide nanosheets grown on Cu foam.[53] Moreover, the CF@FeO_x NAs showed a relatively narrow distribution of pore sizes about 2–5 nm, confirming their mesoporous structure.

The SAED pattern of the FeO_x nanoblock shown in Figure 3e is presented in Figure 3f, which shows the diffraction spots that can be indexed to the (012), (110), and (024) planes of α-Fe_2O_3 and the (220), (400), and (422) planes of Fe_3O_4, indicating a mixed phases of α-Fe_2O_3 and Fe_3O_4. The HRTEM image in Figure 3g shows clear lattice fringes with interlayer spacings of 0.37 and 0.27 nm, which correspond to the (012) and (104) planes of α-Fe_2O_3 (JCPDS card no. 33-0664). In addition, the lattice fringes with interlayer spacings of 0.29 and 0.25 nm, which are assigned to the (220) and (311) planes of Fe_3O_4 (JCPDS card no. 65-3107), respectively, can also be observed (Figure 3h), indicating that the Fe_3O_4 phase was preserved during the annealing process. As a consequence, the obtained FeO_x nanoarrays adopt a mixed iron oxide phases composed of α-Fe_2O_3 and Fe_3O_4. The XRD pattern of the FeO_x powder converted from the precursor powder synthesized without CF under otherwise identical conditions (Figure S2b) suggests that the FeO_x powder contains both α-Fe_2O_3 and Fe_3O_4 phases, as shown in Figure S1b. However, the characteristic peaks of α-Fe_2O_3 and Fe_3O_4 cannot be well resolved from the XRD pattern of the 3D CF@FeO_x NAs because of the strong reflections of copper foam, which overlap the characteristic peaks of FeO_x.

The chemical composition of the 3D CF@FeO_x NAs was further characterized by Raman spectroscopy and SEM-EDS analysis, which are presented in Figure 4. As shown in Figure 4a, the Raman bands at 223 and 493 cm^{-1} correspond to the A_{1g} vibration modes of α-Fe_2O_3, and the four bands at 245, 292, 405, and 615 cm^{-1} can be ascribed to E_g vibration modes of α-Fe_2O_3,[54] indicating the existence of α-Fe_2O_3 in the 3D CF@FeO_x NAs. In addition, the appearance of the Raman bands at 531 and 687 cm^{-1} can be assigned to the vibration modes of Fe_3O_4,[55,56] confirming the coexistence of Fe_3O_4. The SEM image and the corresponding EDS element mapping of the 3D CF@FeO_x NAs are presented in Figure 4b–e, which suggest that the 3D CF@FeO_x NAs actually made of Fe and O

DOI: 10.1021/acsaem.8b01024
ACS Appl. Energy Mater. 2018, 1, 5417–5427

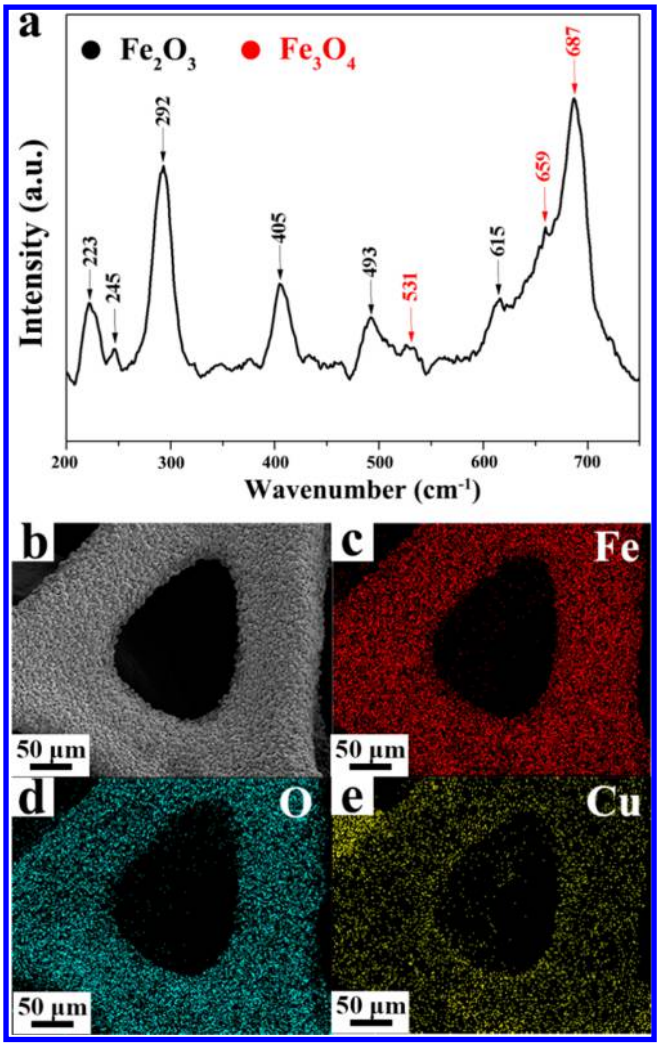

Figure 4. (a) Raman spectrum of 3D CF@FeO_x NAs (the excitation wavelength is 633 nm). SEM image (b) and the corresponding EDS element mappings (c–e) of 3D CF@FeO_x NAs.

together with Cu from the copper foam skeleton. Therefore, it can be concluded that the hierarchical 3D CF@FeO_x NAs consist of porous nanoblock arrays of FeO_x with a mixed α-Fe_2O_3 and Fe_3O_4 phases grown uniformly on the copper foam skeleton.

To determine the contents of α-Fe_2O_3 and Fe_3O_4 in the mixed phases, a piece of the 3D CF@FeO_x NAs plate (0.5 cm × 0.5 cm) was immersed in an aqueous HI solution to dissolve the FeO_x NAs without dissolving the Cu substrate. The mass of the dissolved Fe element was measured using ICP, and the mass of the dissolved FeO_x was calculated by carefully measuring the weight of the 3D CF@FeO_x NAs plate before and after the dissolution. The molar ratio between α-Fe_2O_3 and Fe_3O_4 was calculated to be approximately 1:1, namely, the mass content of α-Fe_2O_3 and Fe_3O_4 in the 3D CF@FeO_x was ~40% and ~60%, respectively. The bare Cu skeleton obtained after dissolving the FeO_x in the 3D CF@FeO_x NAs exhibited rather smooth surfaces and the corresponding EDS spectrum demonstrated the absence of Fe element (Figure S4), confirming that there were no remaining active materials on the copper foam after the dissolution. Furthermore, both the concentrations of the Fe and Cu ions in the dissolved solution were measured by ICP. The measured Fe ion concentration was ~50 μg/mL whereas the Cu ion concentration was only ~0.04 μg/mL, which was less than 0.1% of the Fe concentration, confirming that there was neglectable dissolution of Cu foam in the HI solution and there was essentially no copper oxide existing in the FeO_x NAs. This result strongly indicated that the active materials in the 3D CF@FeO_x NAs were made of α-Fe_2O_3 and Fe_3O_4, and the oxidation of copper foam was neglectable and would not contribute to the capacity if the 3D CF@FeO_x NAs were used as an anode for LIBs. Actually, our preliminary measurement of the electrochemical performance of pure copper foam as an anode for LIBs confirmed that its capacity was neglectable (less than 1 mAh g^{-1}), which is not unexpected since copper foam has been frequently employed as a reliable 3D hierarchical current collector.[57]

To better understand the roles played by different reactants during the hydrothermal process, the effects of the concentrations of $FeSO_4$, urea, and NH_4F in the reactant solutions on the morphology of the annealed products were examined (Figure S5). When the added amount of $FeSO_4 \cdot 7H_2O$ was decreased from 0.6 to 0.3 g, only few FeO_x granules were observed on the surface of copper foam, indicating insufficient Fe source supply (Figure S5a). On the contrary, when the amount of $FeSO_4 \cdot 7H_2O$ was increased to 1.2 g, the size of the FeO_x granules was increased to ~20 μm (Figure S5b). The amount of urea also played a significant role in the morphology of the final product. When the amount of urea was reduced from x to 0.1 g, only few FeO_x granules were grown on the surface of copper foam (Figure S5c). When the amount of urea was increased to 0.4 g, the size of the FeO_x granules was increased to ~20 μm, and there was a significant coalescence between the granules (Figure S 5d). Moreover, the added amount of NH_4F also exhibited significant influence on the growth process. When no NH_4F was added to the reactant solution, there were hardly any FeO_x granules grown on the copper foam (Figure S3e). Nevertheless, if we added a double amount (0.1 g) of NH_4F compared with the typical synthesis conditions, some large spheres appear (Figure S5f). The addition of NH_4F is necessary because F^{-1} ions are beneficial to the adhesion of the precursor to the substrate, as reported previously.[51,58]

It is noteworthy that the annealing time is another import factor that affects the final character of the product. While the typical 3D CF@FeO_x NAs shown in Figure 3 were produced after calcination at 450 °C in Ar atmosphere for 2 h, 3D CF@FeO_x NAs-1 and 3D CF@FeO_x NAs-3 were obtained after annealing for 1 and 3 h, respectively (Figure S6). In contrast to the typical 3D CF@FeO_x NAs, the 3D CF@FeO_x NAs-1 with a less annealing time shows much less pores, indicating incomplete transformation of the precursor to the final FeO_x. However, when the annealing time was extended to 3 h, considerable sintering of nanoparticles constituting the porous FeO_x nanoblocks occurred, leading to the collapse of the porous structure.

The unique structure of the 3D CF@FeO_x NAs may offer direct pathways for electron transport and lithium ion diffusion without the additional binders in addition to enhanced mass loading of the active materials. Accordingly, the obtained 3D CF@FeO_x NAs were used directly as an integrated anode in LIBs and its electrochemical performance was investigated. Figure 5a shows the typical cyclic voltammetric (CV) curves of the 3D CF@FeO_x NAs electrode in the potential window of 0.05–3.0 V with a constant scan rate of 0.1 mV s^{-1}. In the first

DOI: 10.1021/acsaem.8b01024
ACS Appl. Energy Mater. 2018, 1, 5417–5427

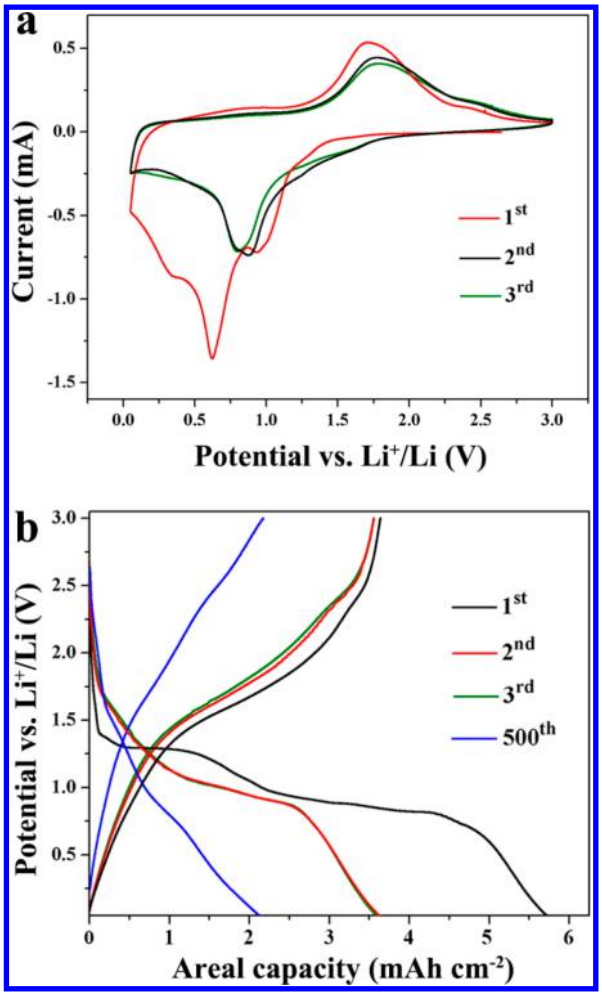

Figure 5. (a) Cyclic voltammetry curves of 3D CF@FeO_x NAs (the scan rate in the initial three cycles is 0.5 mV s^{-1}). (b) Galvanostatic charge−discharge profiles of 3D CF@FeO_x NAs of 1st, 2nd, 3rd, and 500th cycles.

cathodic sweep process, a small reduction peak can be observed at 0.93 V, corresponding to the structural transition induced by lithium ion intercalation to form the Li_yFeO_x ($0 < y < 2$) phase. The sharp peak at 0.62 V is due to the complete reduction of Fe(III) to Fe(0) and the formation of solid electrolyte interphase (SEI).[51] During the anodic sweep process, the broad peaks can be observed at 1.72 V, which are associated with the reversible multiple oxidations of Fe(0) to Fe(II) and Fe(III).[50] Apparently, the CV curves of the second cycle resembled the third one, indicating excellent cycling stability. The shift of the related peaks (reduction peaks at 0.80 V and oxidation peaks at 1.66−1.90 V) to higher potentials (reduction peaks of 0.90 V and oxidation peaks at 1.79 V) in the following two cycles is probably caused by the enhanced charge transfer kinetics resulting from the structural change during the first cycle. Although FeO_x is composed of α-Fe_2O_3 and Fe_3O_4, which have different electrochemical reactions with lithium ions, it is hard to distinguish the peaks arising from α-Fe_2O_3 and Fe_3O_4. The oxidation peak of α-Fe_2O_3 or Fe_3O_4 is usually broad within a voltage window of 1.5−2.0 V, which can be overlapped easily by each other.[51,59] On the other hand, the reduction peaks of α-Fe_2O_3 or Fe_3O_4 are difficult to be figured out because the reduction peaks located at 0.62 and 0.93 V represent the irreversible and reversible formation processes of SEI and Li_xFeO_x, respectively, which have similar electrochemical processes and peak positions for α-Fe_2O_3 and Fe_3O_4.[51,59−62]

The charge−discharge voltage profiles of the 3D CF@FeO_x NAs electrode at the current density of 0.25 mA cm^{-2} (i.e., 0.1 A g^{-1}) in the first three cycles and 2.5 mA cm^{-2} (i.e., 1 A g^{-1}) in the following cycles from 0.05 to 3.0 V are shown in Figure 5b. At the first cycle, the discharge and charge capacities are 5.72 and 3.64 mAh cm^{-2}, respectively, indicating a limited initial Coulombic efficiency of 63.6%. However, the Coulombic efficiency was increased to 98% and 99% in the following second and third cycles. The relatively low initial Coulombic efficiency could be related to the irreversible reactions involved in the inevitable formation of the SEI layer and the degradation of electrolyte, which is a rather common phenomenon for nanostructured electrodes based on porous iron oxide materials.[38,51] During the subsequent cycles, the 3D CF@FeO_x NAs electrode exhibits good cycling performance and maintains a discharge capacity of 2.12 mAh cm^{-2} (i.e., 850.2 mAh g^{-1}) after 500 cycles.

Figure 6a illustrates the rate capability of the 3D CF@FeO_x NAs and FeO_x powder electrodes, which is another indispensable parameter to evaluate an electrode for practical application, especially for high-power energy storage devices.[62] The discharge capacities of the 3D CF@FeO_x NAs electrode are 2.16, 1.59, 1.44, 1.23 mAh cm^{-2} at the current densities of 2.5, 5, 7.5, 10 mA cm^{-2}, respectively. Even at a high current density of 12.5 mA cm^{-2} (i.e., 5 A g^{-1}), the electrode still manifests a discharge capacity of 0.96 mAh cm^{-2}, much higher than that for the FeO_x powder (0.28 mAh cm^{-2}). When the current density returns to 2.5 mA cm^{-2}, the discharge capacity is maintained at 1.77 mAh cm^{-2}, which is superior to the rate capability of the FeO_x powder electrode. The rate capability is closely associated with the charge transfer ability of the electrode. Figure 6b presents the comparative EIS spectra of the 3D CF@FeO_x NAs and FeO_x powder electrodes before cycling. Each plot consists of a sloping line and a semicircle, the diameter of which is associated with the charge transfer resistance on electrode/electrolyte interface (R_{ct}).[51,63] The R_{ct} of the 3D CF@FeO_x NAs electrode (69 Ω) is smaller than that for the FeO_x powder electrode (99 Ω) based on the equivalent circuit model in the inset of Figure 6b, demonstrating better electronic conductivity. Two semicircles appear in the Nyquist plot of the 3D CF@FeO_x NAs after 100 cycles because of the formation of the SEI film (Figure S7). The high frequency one is associated with the resistance caused by the SEI film (R_f), and the adjacent mid frequency one is assigned to R_{ct}. A slight decrease of the R_{ct} from 69 Ω to 65 Ω after cycling may be ascribed to the activation of electrode materials and the full penetration of electrolyte into electrode materials.[63]

The cycling performance of the 3D CF@ FeO_x NAs at 0.25 and 1.25 mA cm^{-2} were shown in Figure 6c. The electrode delivered a high initial discharge areal capacity of 5.75 mAh cm^{-2} at 0.25 mA cm^{-2}. Besides, the areal capacities retained 3.33 mAh cm^{-2} at 0.25 mA cm^{-2} and 2.61 mAh cm^{-2} at 1.25 mA cm^{-2} after 50 cycles, respectively. The corresponding gravimetric capacities are 1332 mAh g^{-1} and 1044 mAh g^{-1}, respectively, which are higher than the theoretical capacities for both α-Fe_2O_3 and Fe_3O_4. This result could be ascribed to the reversible formation of a polymetric/gel-like layer, where excess lithium ions are accommodated at the interfacial sites, which is a common phenomenon for many metal oxides with large exposed surfaces.[49,60,64,65] Comparative investigation of

DOI: 10.1021/acsaem.8b01024
ACS Appl. Energy Mater. 2018, 1, 5417−5427

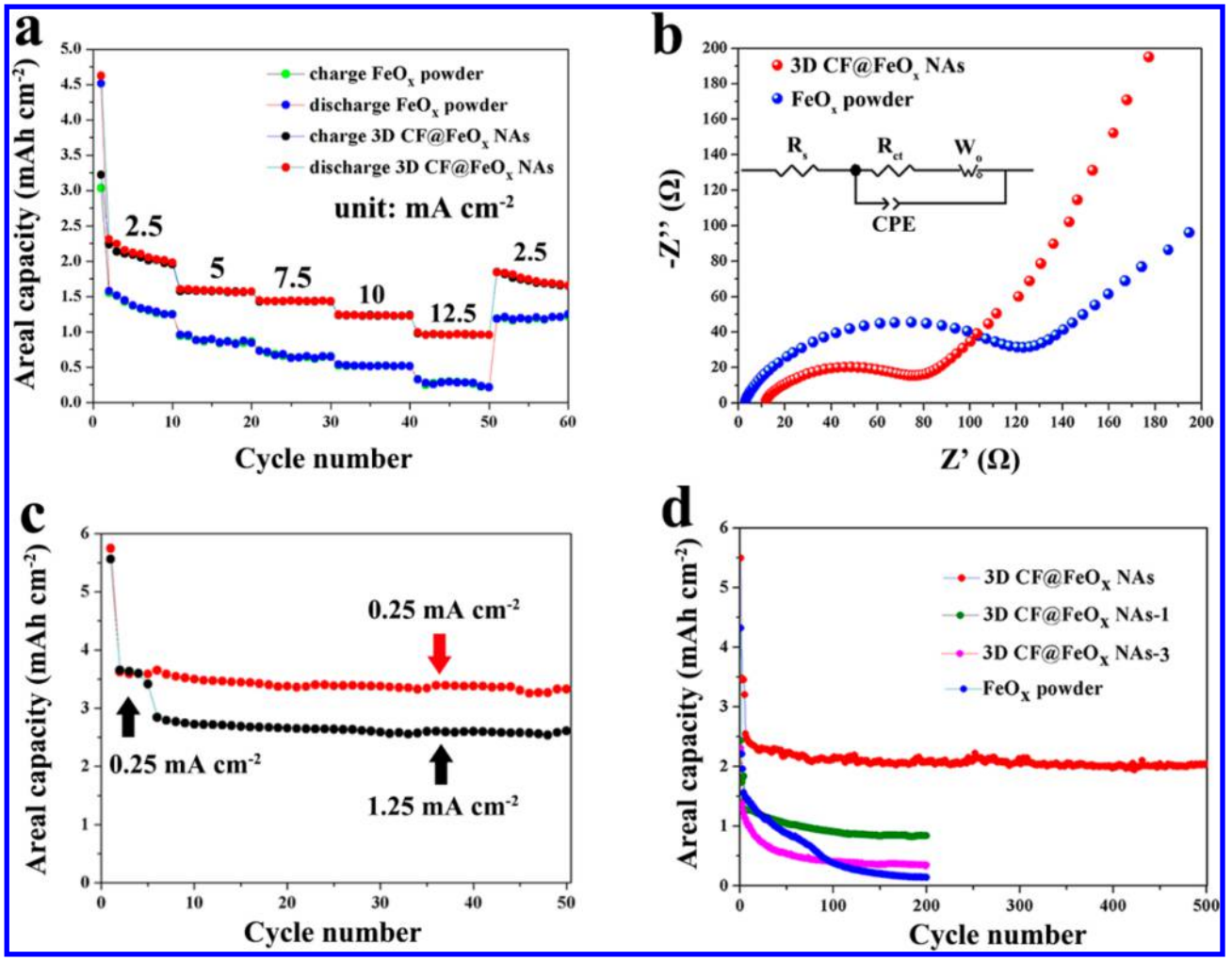

Figure 6. (a) Rate capability of 3D CF@FeO_x NAs at different discharge current densities. The unit of the current density is mA cm^{-2}. (b) EIS spectra of 3D CF@FeO_x NAs and FeO_x powder in range of 10^{-2}–10^5 Hz. The inset is the equivalent circuit used to interpret the data. (c) Cycling performance of 3D CF@FeO_x NAs at 0.25 and 1.25 mA cm^{-2} (the current density is 0.25 mA cm^{-2} in the initial five cycles for activation). (d) Cycling performance of 3D CF@FeO_x NAs-1, 3D CF@FeO_x NAs-3, and FeO_x powder electrodes at 0.25 mA cm^{-2} in the initial five cycles and 2.5 mA cm^{-2} at the following cycles.

the long-term cycling stability of the 3D CF@ FeO_x NAs was carried out, which is shown in Figure 6d. For comparison, the 3D CF@ FeO_x NAs-1, 3D CF@ FeO_x NAs-3, and FeO_x powder electrodes as control examples were also tested. Impressively, the 3D CF@FeO_x NAs electrode can cycle steadily for 500 cycles with an areal capacity as high as 2.12 mAh cm^{-2} at 2.5 mA cm^{-2} (i.e., 1 A g^{-1}), corresponding to a capacity retention ratio of 58.2%. To the best of our knowledge, the electrochemical performance of the 3D CF@ FeO_x NAs is the best for the iron oxide-based electrodes in terms of areal capacity (Table S1). Particularly, the areal capacity of the 3D CF@FeO_x NAs is better than those reported for the α-Fe_2O_3 multishelled hollow microspheres (1.02 mAh cm^{-2} at 0.03 mA cm^{-2}),[17] α-Fe_2O_3/carbon nanotube-graphene foam (1.2 mAh cm^{-2} at 0.24 mA cm^{-2}),[42] and graphene paper@Fe_3O_4 nanorod array@ graphene (1.81 mAh cm^{-2} at 0.75 mA cm^{-2}).[41] In contrast, the FeO_x powder electrode shows severe capacity decay with a low areal capacity of 0.15 mAh cm^{-2} retained only after 200 cycles under the same current density. Besides, the electrodes fabricated with double amounts of $FeSO_4$ and urea show poor cycling performance (Figure S8), which can be rationalized by considering that the FeO_x granules with larger diameters are unfavorable for the lithium ion transport, and the lack of interspaces between FeO_x granules tend to cause the pulverization of the electrode (Figure S5). Beyond that, the 3D CF@FeO_x NAs-1 and 3D CF@ FeO_x NAs-3 electrodes also show inferior cycling performance. The incomplete transformation of the precursor and the less pores for the 3D CF@ FeO_x NAs-1 electrode could result in relatively less active materials and less efficient penetration of the electrolyte into the interior of FeO_x, leading to a lower capacity (0.88 mAh cm^{-2}, 200 cycles). Similarly, the collapse of the porous structure in the 3D CF@FeO_x NAs-3 electrode due to considerable sintering gives rise to blocked electrolyte penetration and poor cycling stability (0.36 mAh cm^{-2}, 200 cycles).

Figure 7 shows the morphology and structure of the fully discharged 3D CF@FeO_x NAs electrode after 500 cycles. On the basis of the SEM image in Figure 7a, the integrity of the FeO_x granules is maintained without structural collapse and crack. However, the original FeO_x nanoblocks became nanoparticle agglomerates without regular shapes and sharp edges (Figure 7b). Figure 7c is the TEM image, the measured

DOI: 10.1021/acsaem.8b01024
ACS Appl. Energy Mater. 2018, 1, 5417–5427

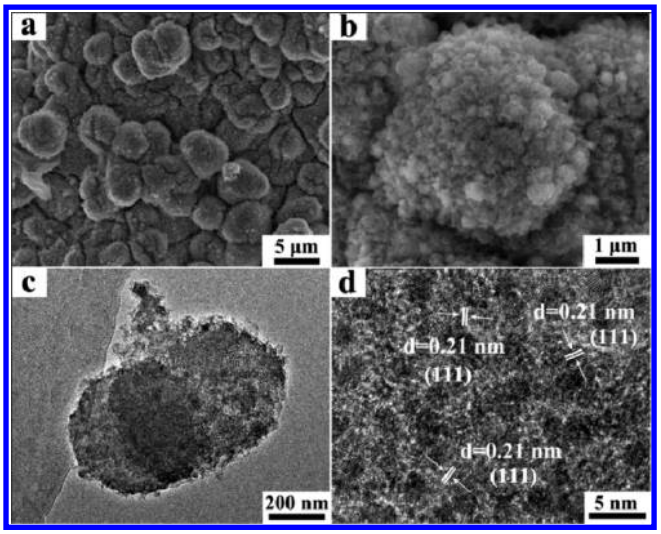

Figure 7. SEM (a, b) and TEM (c, d) images of 3D CF@FeO_x NAs electrode after 500 cycles. 0.25 mA cm^{-2} in the initial five cycles and 2.5 mA cm^{-2} at the following cycles.

interlayer spacings are 0.21 nm from the HRTEM image shown in Figure 7d, which can be assigned to the (111) planes of metallic Fe (JCPDS card no. 65-4150), indicating homogeneous distribution of Fe in amorphous Li_2O to form a continuous conductive metallic network, which is beneficial for the electron transport. The improved cycling stability of the 3D CF@FeO_x NAs electrode may be attributed to the following aspects: First, the tight contact between the FeO_x granules and the copper foam current collector offers the direct electron pathways for electrons with high transport efficiency. Second, the unique hierarchical porous structure of FeO_x nanoarrays allows for efficient penetration of electrolyte with enhanced lithium ion diffusion rate, and the leisure space between neighboring nanoparticles is beneficial to alleviate the huge volume expansion of FeO_x during charge and discharge processes. Third, the 3D CF skeleton supplies more growth sites for loading FeO_x with a high loading mass, leading to improved whole energy of the electrode. Last but not least, the absence of insulating binders and the formation of metal Fe continuous conductive network guarantee the high electrical conductivity of the electrode.

To better estimate the potential for real world utilization, we assembled a lithium full cell with $LiNi_{0.8}Co_{0.15}Al_{0.05}$ (NCA) as a cathode[52] and 3D CF@FeO_x NAs as an anode, as shown in Figure 8a. Considering that the capacity of the 3D CF@FeO_x NAs anode after 50 cycles at 0.1 A g^{-1} (1332 mAh g^{-1}) is ~8 times higher than that of the NCA cathode after 50 cycles under the similar current density (~165 mAh g^{-1}),[52] the active material mass ratio of the anode to cathode was fixed to be 1:10 with a slightly increased cathode/anode weight ratio to make up the irreversible Li^+ loss for forming SEI film on 3D CF@FeO_x NAs electrode. The full cell was cycled at 2.5 mA cm^{-2} for 50 cycles in the voltage window of 1.0−3.75 V. The 1st, 2nd, 3rd, and 50th charge−discharge profiles are presented in Figure 8b, which shows that the initial charge and discharge capacities are 4.20 and 2.20 mAh cm^{-2}, respectively. As shown in Figure 8c, the 3D CF@FeO_x NAs electrode of the full cell maintained discharge capacities of 1.06 mAh cm^{-2} (capacity retention ~ 48.2%) after 30 cycles and 0.94 mAh cm^{-2} (capacity retention ~ 42.7%) after 50 cycles. A continuous capacity loss with cycling occurred, and the capacity was decreased gradually to 0.38 mAh cm^{-2} (capacity retention ~ 17.3%) after 200 cycles (Figure S9). Compared with the lithium full cell assembled by using 3D hierarchical porous α-Fe_2O_3 nanosheets on copper foil as the anode, which maintained a discharge capacity of ~0.15 mAh cm^{-2} (capacity retention ~ 52.7%) after 30 cycles,[50] the current full cell assembled using the 3D CF@FeO_x NAs as the anode exhibited comparable cycling stability and a significantly enhanced areal capacity. The capacity fading with cycling may be ascribed to a variety of factors, such as the selected voltage window, electrolyte, cathode, and mass ratio of active materials between the cathode and the anode. Although the cyclability is still far from the requirements for practical applications, it may represent a beneficial attempt toward practicality. Undoubtedly, further efforts are needed to optimize the cell parameters to achieve high-performance full cells with high areal capacity and high cyclability.

4. CONCLUSIONS

In summary, hierarchical porous FeO_x nanoarrays were directly constructed on 3D copper foam through facile hydrothermal growth followed by postannealing processes. The resultant 3D CF@FeO_x NAs with a high FeO_x loading density of 2.5 mg cm^{-2} were tested as a novel integrated anode for LIBs, which demonstrated a high areal capacity of 2.12 mAh cm^{-2} after 500 cycles at 2.5 mA cm^{-2}. A remarkable rate capability of the 3D CF@FeO_x NAs was achieved with an areal capacity of 0.96

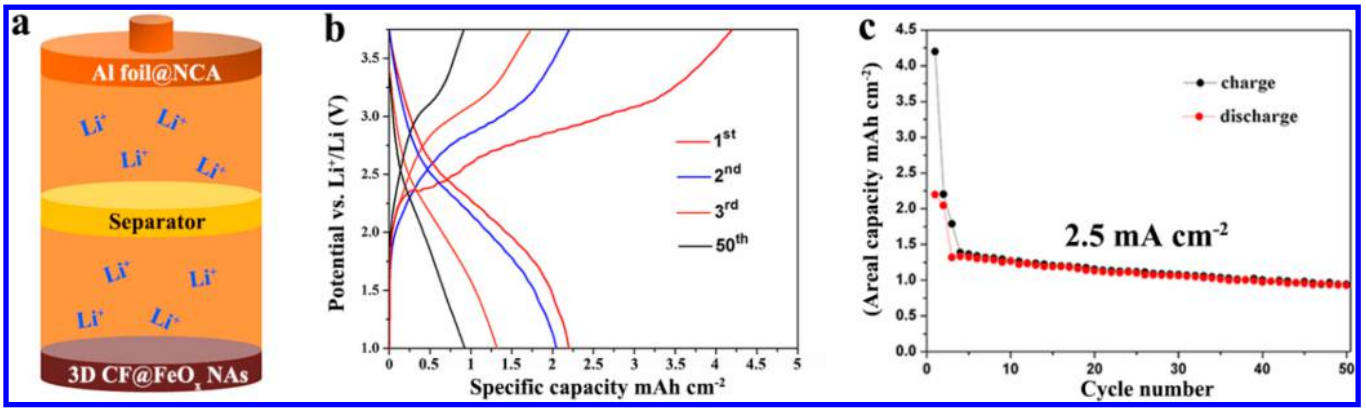

Figure 8. (a) Schematic illustration of a 3D CF@FeO_x NAs//Al@NCA LIB device. (b) Galvanostatic charge−discharge voltage profiles and (c) cycling performance of a 3D CF@FeO_x NAs//Al@NCA lithium ion full cell at 2.5 mA cm^{-2}. The voltage window is 1.0−3.75 V.

DOI: 10.1021/acsaem.8b01024
ACS Appl. Energy Mater. 2018, 1, 5417−5427

mAh cm^{-2} at a higher current density of 12.5 mA cm^{-2} (i.e., 5 A g^{-1}). To our knowledge, the 3D CF@FeO_x NAs exhibited the best electrochemical performance with respect to the areal capacity among the iron oxide-based electrodes. The excellent electrochemical performance can be attributed to the unique merits of the 3D electrode with hierarchical nanoarrays of FeO_x: (1) the good contact between FeO_x nanoarrays and CF, as well as the absence of binder provides direct pathways for electrons transport; (2) the hierarchical FeO_x nanostructures with porous structure offer sufficient penetration of the electrolyte with reduced lithium ions diffusion lengths, as well as alleviates the volume expansion of FeO_x; and (3) the more growth sites supplied by 3D CF ensure a high loading mass of FeO_x, leading to enhanced areal capacity. The lithium full cell test manifests the promising potential of 3D CF@FeO_x NAs for practical utilization. The fabrication method provides a promising way to construct high-areal-capacity electrodes for the next-generation energy storage devices.

■ ASSOCIATED CONTENT

Supporting Information

The Supporting Information is available free of charge on the ACS Publications website at DOI: 10.1021/acsaem.8b01024.

Additional XRD, SEM, and electrochemical characterizations of the 3D CF@FeO_x NAs and a table summarizing the reported areal capacities for the iron oxide electrodes (PDF)

■ AUTHOR INFORMATION

Corresponding Authors

*E-mail: liminqi@pku.edu.cn.
*E-mail: hhzhou@pku.edu.cn.

ORCID

Limin Qi: 0000-0003-4959-6928

Author Contributions

‡F.Z. and C.Y. contributed equally.

Notes

The authors declare no competing financial interest.

■ ACKNOWLEDGMENTS

This work was financially supported by NSFC (Grant Nos. 21473004 and 21673007).

■ REFERENCES

(1) Armand, M.; Tarascon, J. M. Building Better Batteries. *Nature* **2008**, *451*, 652−657.
(2) Van Noorden, R. The Rechargeable Revolution: A Better Battery. *Nature* **2014**, *507*, 26−28.
(3) Larcher, D.; Tarascon, J. M. Towards Greener and More Sustainable Batteries for Electrical Energy Storage. *Nat. Chem.* **2015**, *7*, 19−29.
(4) Ji, L.; Lin, Z.; Alcoutlabi, M.; Zhang, X. Recent Developments in Nanostructured Anode Materials for Rechargeable Lithium-Ion Batteries. *Energy Environ. Sci.* **2011**, *4*, 2682−2699.
(5) Reddy, M. V.; Subba Rao, G. V.; Chowdari, B. V. Metal Oxides and Oxysalts as Anode Materials for Li Ion Batteries. *Chem. Rev.* **2013**, *113*, 5364−457.
(6) Cabana, J.; Monconduit, L.; Larcher, D.; Palacin, M. R. Beyond Intercalation-Based Li-Ion Batteries: The State of The Art and Challenges of Electrode Materials Reacting Through Conversion Reactions. *Adv. Mater.* **2010**, *22*, E170−E192.
(7) Zhang, L.; Wu, H. B.; Lou, X. W. D. Iron-Oxide-Based Advanced Anode Materials for Lithium-Ion Batteries. *Adv. Energy Mater.* **2014**, *4*, 1300958.
(8) Keppeler, M.; Shen, N.; Nageswaran, S.; Srinivasan, M. Synthesis of α-Fe_2O_3/Carbon Nanocomposites as High Capacity Electrodes for Next Generation Lithium Ion Batteries: A Review. *J. Mater. Chem. A* **2016**, *4*, 18223−18239.
(9) Jiang, J.; Li, Y.; Liu, J.; Huang, X.; Yuan, C.; Lou, X. W. Recent Advances in Metal Oxide-Based Electrode Architecture Design for Electrochemical Energy Storage. *Adv. Mater.* **2012**, *24*, 5166−5180.
(10) Roy, P.; Srivastava, S. K. Nanostructured Anode Materials for Lithium Ion Batteries. *J. Mater. Chem. A* **2015**, *3*, 2454−2484.
(11) Aravindan, V.; Lee, Y.-S.; Madhavi, S. Research Progress on Negative Electrodes for Practical Li-Ion Batteries: Beyond Carbonaceous Anodes. *Adv. Energy Mater.* **2015**, *5*, 1402225.
(12) Wang, Z.; Liu, C. J. Preparation and Application of Iron Oxide/Graphene Based Composites for Electrochemical Energy Storage and Energy Conversion Devices: Current Status and Perspective. *Nano Energy* **2015**, *11*, 277−293.
(13) Zhu, J.; Yin, Z.; Yang, D.; Sun, T.; Yu, H.; Hoster, H. E.; Hng, H. H.; Zhang, H.; Yan, Q. Hierarchical Hollow Spheres Composed of Ultrathin Fe_2O_3 Nanosheets for Lithium Storage and Photocatalytic Water Oxidation. *Energy Environ. Sci.* **2013**, *6*, 987−993.
(14) Zhou, L.; Xu, H.; Zhang, H.; Yang, J.; Hartono, S. B.; Qian, K.; Zou, J.; Yu, C. Cheap and Scalable Synthesis of α-Fe_2O_3 Multi-Shelled Hollow Spheres as High-Performance Anode Materials for Lithium Ion Batteries. *Chem. Commun.* **2013**, *49*, 8695−8697.
(15) Wang, B.; Wu, H. B.; Zhang, L.; Lou, X. W. Self-Supported Construction of Uniform Fe_3O_4 Hollow Microspheres from Nanoplate Building Blocks. *Angew. Chem., Int. Ed.* **2013**, *52*, 4165−4168.
(16) Banerjee, A.; Aravindan, V.; Bhatnagar, S.; Mhamane, D.; Madhavi, S.; Ogale, S. Superior Lithium Storage Properties of α-Fe_2O_3 Nano-Assembled Spindles. *Nano Energy* **2013**, *2*, 890−896.
(17) Xu, S.; Hessel, C. M.; Ren, H.; Yu, R.; Jin, Q.; Yang, M.; Zhao, H.; Wang, D. α-Fe_2O_3 Multi-Shelled Hollow Microspheres for Lithium Ion Battery Anodes with Superior Cpacity and Charge Retention. *Energy Environ. Sci.* **2014**, *7*, 632−637.
(18) Xu, Y.; Jian, G.; Liu, Y.; Zhu, Y.; Zachariah, M. R.; Wang, C. Superior Electrochemical Performance and Structure Evolution of Mesoporous Fe_2O_3 Anodes for Lithium-Ion Batteries. *Nano Energy* **2014**, *3*, 26−35.
(19) Huang, W.; Xiao, X.; Engelbrekt, C.; Zhang, M.; Li, S.; Ulstrup, J.; Ci, L.; Feng, J.; Si, P.; Chi, Q. Graphene Encapsulated Fe_3O_4 Nanorods Assembled into A Mesoporous Hybrid Composite Used as A High-Performance Lithium-Ion Battery Anode Material. *Mater. Chem. Front.* **2017**, *1*, 1185−1193.
(20) Wang, J.; Tang, H.; Wang, H.; Yu, R.; Wang, D. Multi-Shelled Hollow Micro-/Nanostructures: Promising Platforms for Lithium-Ion Batteries. *Mater. Chem. Front.* **2017**, *1*, 414−430.
(21) Qi, J.; Lai, X.; Wang, J.; Tang, H.; Ren, H.; Yang, Y.; Jin, Q.; Zhang, L.; Yu, R.; Ma, G.; Su, Z.; Zhao, H.; Wang, D. Multi-Shelled Hollow Micro-/Nanostructures. *Chem. Soc. Rev.* **2015**, *44*, 6749−6773.
(22) Li, H.; Ma, H.; Yang, M.; Wang, B.; Shao, H.; Wang, L.; Yu, R.; Wang, D. Highly Controlled Synthesis of Multi-Shelled NiO Hollow Microspheres for Enhanced Lithium Storage Properties. *Mater. Res. Bull.* **2017**, *87*, 224−229.
(23) Zhang, J.; Ren, H.; Wang, J.; Qi, J.; Yu, R.; Wang, D.; Liu, Y. Engineering of Multi-Shelled SnO_2 Hollow Microspheres for Highly Stable Lithium-Ion Batteries. *J. Mater. Chem. A* **2016**, *4*, 17673−17677.
(24) Wang, F.; Wang, J.; Ren, H.; Tang, H.; Yu, R.; Wang, D. Multi-Shelled $LiMn_2O_4$ Hollow Microspheres as Superior Cathode Materials for Lithium-Ion Batteries. *Inorg. Chem. Front.* **2016**, *3*, 365−369.
(25) Ren, H.; Sun, J.; Yu, R.; Yang, M.; Gu, L.; Liu, P.; Zhao, H.; Kisailus, D.; Wang, D. Controllable Synthesis of Mesostructures from TiO_2 Hollow to Porous Nanospheres with Superior Rate Performance for Lithium Ion Batteries. *Chem. Sci.* **2016**, *7*, 793−798.

DOI: 10.1021/acsaem.8b01024
ACS Appl. Energy Mater. 2018, 1, 5417−5427

(26) Zhao, X.; Yu, R.; Tang, H.; Mao, D.; Qi, J.; Wang, B.; Zhang, Y.; Zhao, H.; Hu, W.; Wang, D. Formation of Septuple-Shelled $(Co_{2/3}Mn_{1/3})(Co_{5/6}Mn_{1/6})_2O_4$ Hollow Spheres as Electrode Material for Alkaline Rechargeable Battery. *Adv. Mater.* **2017**, *29*, 1700550.
(27) Wang, J.; Yang, N.; Tang, H.; Dong, Z.; Jin, Q.; Yang, M.; Kisailus, D.; Zhao, H.; Tang, Z.; Wang, D. Accurate Control of Multishelled Co_3O_4 Hollow Microspheres as High-Performance Anode Materials in Lithium-Ion Batteries. *Angew. Chem., Int. Ed.* **2013**, *52*, 6417−6420.
(28) Wang, B.; Lu, X. Y.; Wong, K. Y.; Tang, Y. Facile Solvothermal Synthesis and Superior Lithium Storage Capability of Co_3O_4 Nanoflowers with Multi-Scale Dimensions. *Mater. Chem. Front.* **2017**, *1*, 468−476.
(29) Li, J. Y.; Xu, Q.; Li, G.; Yin, Y.-X.; Wan, L. J.; Guo, Y. G. Research Progress Regarding Si-Based Anode Materials Towards Practical Application in High Energy Density Li-Ion Batteries. *Mater. Chem. Front.* **2017**, *1*, 1691−1708.
(30) Ma, F. X.; Hu, H.; Wu, H. B.; Xu, C. Y.; Xu, Z.; Zhen, L.; Lou, X. W. Formation of Uniform Fe_3O_4 Hollow Spheres Organized by Ultrathin Nanosheets and Their Excellent Lithium Storage Properties. *Adv. Mater.* **2015**, *27*, 4097−4101.
(31) Wei, W.; Yang, S.; Zhou, H.; Lieberwirth, I.; Feng, X.; Mullen, K. 3D Graphene Foams Cross-Linked with Pre-Encapsulated Fe_3O_4 Nanospheres for Enhanced Lithium Storage. *Adv. Mater.* **2013**, *25*, 2909−2914.
(32) Xiao, L.; Wu, D.; Han, S.; Huang, Y.; Li, S.; He, M.; Zhang, F.; Feng, X. Self-Assembled Fe_2O_3/Graphene Aerogel with High Lithium Storage Performance. *ACS Appl. Mater. Interfaces* **2013**, *5*, 3764−3769.
(33) Chen, S.; Bao, P.; Wang, G. Synthesis of Fe_2O_3−CNT−Graphene Hybrid Materials with An Open Three-Dimensional Nanostructure for High Capacity Lithium Storage. *Nano Energy* **2013**, *2*, 425−434.
(34) Luo, J.; Liu, J.; Zeng, Z.; Ng, C. F.; Ma, L.; Zhang, H.; Lin, J.; Shen, Z.; Fan, H. J. Three-Dimensional Graphene Foam Supported Fe_3O_4 Lithium Battery Anodes with Long Cycle Life and High Rate Capability. *Nano Lett.* **2013**, *13*, 6136−6143.
(35) Jian, Z.; Zhao, B.; Liu, P.; Li, F.; Zheng, M.; Chen, M.; Shi, Y.; Zhou, H. Fe_2O_3 Nanocrystals Anchored onto Graphene Nanosheets as The Anode Material for Low-Cost Sodium-Ion Batteries. *Chem. Commun.* **2014**, *50*, 1215−1217.
(36) Li, Y.; Zhang, H.; Kang Shen, P. Ultrasmall Metal Oxide Nanoparticles Anchored on Three-Dimensional Hierarchical Porous Gaphene-Like Networks as Anode for High-Performance Lithium Ion Batteries. *Nano Energy* **2015**, *13*, 563−572.
(37) Liu, M.; Ma, X.; Gan, L.; Xu, Z.; Zhu, D.; Chen, L. A Facile Synthesis of A Novel Mesoporous Ge@C Sphere Anode with Stable and High Capacity for Lithium Ion Batteries. *J. Mater. Chem. A* **2014**, *2*, 17107−17114.
(38) Jiang, T.; Bu, F.; Feng, X.; Shakir, I.; Hao, G.; Xu, Y. Porous Fe_2O_3 Nanoframeworks Encapsulated within Three-Dimensional Graphene as High-Performance Flexible Anode for Lithium-Ion Battery. *ACS Nano* **2017**, *11*, 5140−5147.
(39) Fan, L.; Li, B.; Rooney, D. W.; Zhang, N.; Sun, K. In Situ Preparation of 3D Graphene Aerogels@Hierarchical Fe_3O_4 Nanoclusters as High Rate and Long Cycle Anode Materials for Lithium Ion Batteries. *Chem. Commun.* **2015**, *51*, 1597−1600.
(40) Jiang, X.; Yang, X.; Zhu, Y.; Yao, Y.; Zhao, P.; Li, C. Graphene/Carbon-Coated Fe_3O_4 Nanoparticle Hybrids for Enhanced Lithium Storage. *J. Mater. Chem. A* **2015**, *3*, 2361−2369.
(41) Jiang, Y.; Jiang, Z.-J.; Yang, L.; Cheng, S.; Liu, M. A High-Performance Anode for Lithium Ion Batteries: Fe_3O_4 Microspheres Encapsulated in Hollow Graphene Shells. *J. Mater. Chem. A* **2015**, *3*, 11847−11856.
(42) Guo, J.; Zhu, H.; Sun, Y.; Zhang, X. Construction of Sandwiched Graphene Paper@Fe_3O_4 Nanorod Array@Graphene for Large and Fast Lithium Storage with An Extended Lifespan. *J. Mater. Chem. A* **2015**, *3*, 19384−19392.
(43) Chen, M.; Liu, J.; Chao, D.; Wang, J.; Yin, J.; Lin, J.; Jin Fan, H.; Xiang Shen, Z. Porous α-Fe_2O_3 Nanorods Supported on Carbon Nanotubes-Graphene Foam as Superior Anode for Lithium Ion Batteries. *Nano Energy* **2014**, *9*, 364−372.
(44) Chabi, S.; Peng, C.; Hu, D.; Zhu, Y. Ideal Three-Dimensional Electrode Structures for Electrochemical Energy Etorage. *Adv. Mater.* **2014**, *26*, 2440−2445.
(45) Ellis, B. L.; Knauth, P.; Djenizian, T. Three-Dimensional Self-Supported Metal Oxides for Advanced Energy Storage. *Adv. Mater.* **2014**, *26*, 3368−3397.
(46) Zhang, F.; Qi, L. Recent Progress in Self-Supported Metal Oxide Nanoarray Electrodes for Advanced Lithium-Ion Batteries. *Adv. Sci.* **2016**, *3*, 1600049.
(47) Zhao, H.; Zhou, M.; Wen, L.; Lei, Y. Template-Directed Construction of Nanostructure Arrays for Highly-Efficient Energy Storage and Conversion. *Nano Energy* **2015**, *13*, 790−813.
(48) Wang, Z.; Cao, D.; Xu, R.; Qu, S.; Wang, Z.; Lei, Y. Realizing Ordered Arrays of Nanostructures: A Versatile Platform for Converting and Storing Energy Efficiently. *Nano Energy* **2016**, *19*, 328−362.
(49) Jiang, Y.; Zhang, D.; Li, Y.; Yuan, T.; Bahlawane, N.; Liang, C.; Sun, W.; Lu, Y.; Yan, M. Amorphous Fe_2O_3 as A High-Capacity, High-Rate and Long-Life Anode Material for Lithium Ion Batteries. *Nano Energy* **2014**, *4*, 23−30.
(50) Chen, S.; Xin, Y.; Zhou, Y.; Zhang, F.; Ma, Y.; Zhou, H.; Qi, L. Robust α-Fe_2O_3 Nanorod Arrays with Optimized Interstices as High-Performance 3D Anodes for High-Rate Lithium Ion Batteries. *J. Mater. Chem. A* **2015**, *3*, 13377−13383.
(51) Cao, K.; Jiao, L.; Liu, H.; Liu, Y.; Wang, Y.; Guo, Z.; Yuan, H. 3D Hierarchical Porous α-Fe_2O_3 Nanosheets for High-Performance Lithium-Ion Batteries. *Adv. Energy Mater.* **2015**, *5*, 1401421.
(52) Yang, C.; Shao, R.; Mi, Y.; Shen, L.; Zhao, B.; Wang, Q.; Wu, K.; Lui, W.; Gao, P.; Zhou, H. Stable Interstitial Layer to Alleviate Fatigue Fracture of High Nickel Cathode for Lithium-Ion Batteries. *J. Power Sources* **2018**, *376*, 200−206.
(53) Liu, Y.; Teng, X.; Mi, Y.; Chen, Z. A New Architecture Design of Ni−Co LDH-Based Pseudocapacitors. *J. Mater. Chem. A* **2017**, *5*, 24407−24415.
(54) de Faria, D. L. A.; Venâncio Silva, S.; de Oliveira, M. T. Raman Microspectroscopy of Some Iron Oxides and Oxyhydroxides. *J. Raman Spectrosc.* **1997**, *28*, 873−878.
(55) Nasibulin, A. G.; Rackauskas, S.; Jiang, H.; Tian, Y.; Mudimela, P. R.; Shandakov, S. D.; Nasibulina, L. I.; Jani, S.; Kauppinen, E. I. Simple and Rapid Synthesis of α-Fe_2O_3 Nanowires under Ambient Conditions. *Nano Res.* **2009**, *2*, 373−379.
(56) Mohamed, M. M.; Bayoumy, W. A.; Goher, M. E.; Abdo, M. H.; Mansour El-Ashkar, T. Y. Optimization of α-Fe_2O_3@Fe_3O_4 Incorporated N-TiO_2 as Super Effective Photocatalysts under Visible Light Irradiation. *Appl. Surf. Sci.* **2017**, *412*, 668−682.
(57) Yue, Y.; Liang, H. 3D Current Collectors for Lithium-Ion Batteries: A Topical Review. *Small Methods* **2018**, *2*, 1800056.
(58) Xu, W.; Zhao, K.; Niu, C.; Zhang, L.; Cai, Z.; Han, C.; He, L.; Shen, T.; Yan, M.; Qu, L.; Mai, L. Heterogeneous Branched Core−Shell SnO_2−PANI Nanorod Arrays with Mechanical Integrity and Three Dimentional Electron Transport for Lithium Batteries. *Nano Energy* **2014**, *8*, 196−204.
(59) Zuo, Y.; Wang, G.; Peng, J.; Li, G.; Ma, Y.; Yu, F.; Dai, B.; Guo, Xu.; Wong, C. Hybridization of Graphene Nanosheets and Carbon-coated Hollow Fe_3O_4 Nanoparticles as A High Performance Anode Material for Lithium-Ion Batteries. *J. Mater. Chem. A* **2016**, *4*, 2453−2460.
(60) Jayaraman, S.; Aravindan, V.; Ulaganathan, M.; Ling, W.; Ramakrishna, S.; Madhavi, S. Ultralong Durability of Porous α-Fe_2O_3 Nanofibers in Practical Li-Ion Configuration with $LiMn_2O_4$ Cathode. *Adv. Sci.* **2015**, *2*, 1500050.
(61) Liu, L.; Yang, X.; Lv, C.; Zhu, A.; Zhu, X.; Guo, S.; Chen, C.; Yang, D. Seaweed-Derived Route to Fe_2O_3 Hollow Nanoparticles/N-Doped Graphene Aerogels with High Lithium Ion Storage Performance. *ACS Appl. Mater. Interfaces* **2016**, *8*, 7047−7053.

DOI: 10.1021/acsaem.8b01024
ACS Appl. Energy Mater. 2018, 1, 5417−5427

(62) Tang, Y.; Zhang, Y.; Li, W.; Ma, B.; Chen, X. Rational Material Design for Ultrafast Rechargeable Lithium-Ion Batteries. *Chem. Soc. Rev.* **2015**, *44*, 5926−5940.
(63) Zhang, Y.-C.; You, Y.; Xin, S.; Yin, Y.-X.; Zhang, J.; Wang, P.; Zheng, X.-S.; Cao, F.-F.; Guo, Y.-G. Rice Husk-Derived Hierarchical Silicon/Nitrogen-Doped Carbon/Carbon Nanotube Spheres as Low-Cost and High-Capacity Anodes for Lithium-Ion Batteries. *Nano Energy* **2016**, *25*, 120−127.
(64) Shin, J.; Samuelis, D.; Maier, J. Sustained Lithium-Storage Performance of Hierarchical, Nanoporous Anatase TiO_2 at High Rates: Emphasis on Interfacial Storage Phenomena. *Adv. Funct. Mater.* **2011**, *21*, 3464−3472.
(65) Wang, X.; Tian, W.; Liu, D.; Zhi, C.; Bando, Y.; Golberg, D. Unusual Formation of α-Fe_2O_3 Hexagonal Nanoplatelets in N-Doped Sandwiched Graphene Chamber for High-Performance Lithium-Ions Batterie. *Nano Energy* **2013**, *2* (2), 257−267.

DOI: 10.1021/acsaem.8b01024
ACS Appl. Energy Mater. 2018, 1, 5417−5427